Neural Network Boundary Detection for 3D Vessel Segmentation

Robert Ieuan Palmer and Xianghua Xie

Department of Computer Science, Swansea University, UK

Abstract. Conventionally, hand-crafted features are used to train machine learning algorithms, however choosing useful features is not a trivial task as they are very much data-dependent. Given raw image intensities as inputs, supervised neural networks (NNs) essentially learn useful features by adjusting the weights of its nodes using the *back-propagation* algorithm. In this paper we investigate the performance of NN architectures for the purpose of boundary detection, before integrating a chosen architecture in a data-driven deformable modelling framework for full segmentation. Boundary detection performed well, with boundary sensitivity of $> 88\%$ and specificity of $> 85\%$ for highly obscured and diffused lymphatic vessel walls. In addition, the vast majority of all boundary-classified pixels were in the immediate vicinity of the ground truth boundary. When integrated into a 3D deformable modelling framework it produced an area overlap with the ground truth of $> 98\%$, and both point-to-mesh and Hausdorff distance errors were less than other approaches. To this end it has been shown that NNs are suitable for boundary detection in deformable modelling, where object boundaries are obscured, diffused and low in contrast.

1 Introduction

Deformable models are popular techniques for both image segmentation [18–20, 12, 13, 5, 14, 6] and tracking [1], and have also been used specifically for vessel segmentation [21, 2, 4, 9, 7, 3]. Typically, an initial model is aligned with a test image before being deformed to fit the object boundary. By using bottom-up data-driven constraints as well as top-down prior shape knowledge, they have the ability to overcome appearance inconsistencies which are often present in images from numerous modalities.

To avoid contour entanglement, search paths are regularly defined along the surface normal direction for each of the initial contour points. The search path coordinates with the strongest boundary responses are then taken as the contour points' new position. Learning-based boundary detectors are therefore often necessary in order to drive the initial model towards the object boundary, and have been used in medical image deformable modelling [12, 15, 11]. Often, these studies consist of hand-picking useful features to distinguish between boundary and non-boundary pixels, e.g. Haar features [15], and gradient steerable features [11]. However, choosing appropriate features to use is not a trivial task as useful

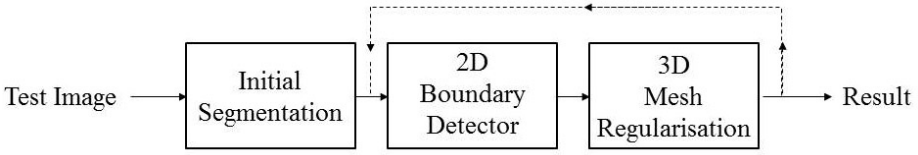

Fig. 1. Overview of the proposed lymphatic vessel segmentation at the testing stage.

features are very much data-dependent, with object type, image modality and image contrast all effecting the usefulness of a feature. In addition, highly abstract features may be very useful for boundary detection, therefore by using hand-crafted features it is possible to miss out on some additional, potentially useful information.

Multilayer NNs are composed of multiple processing layers which are themselves composed of multiple nodes that are interconnected by weighted connections. An error is computed by comparing the *forward-propagation* of the inputs through the network with the desired output, and the *back-propagation* algorithm is implemented to adjust the weights. The network therefore fits a function to a supervised output given the input values and output prediction, essentially learning abstract representations of the input data. As a result, the weight of each node is essentially an individual feature, meaning the network is capable of learning useful features. For these reasons NNs are popular learning systems for image recognition, and have been used specifically for edge detection [16, 10].

Due to the nature of the imaging modality, slices tend to have a highly prominent boundary appearance on the left hand side of the vessel, whereas they are extremely obscure to the right hand side. This makes choosing features capable of identifying all boundary pixels very challenging. We propose inputting raw intensity values into a neural network to be used as a learning-based boundary detector for deformable model-based segmentation. We perform experiments on ex-vivo confocal microscopy images of the lymphatic vessel, where vessel walls are very low in contrast with many weak edges. Pixels are classified as being on the vessel's outer wall or not, and mesh regularisation is used for complete 3D segmentation.

2 Method

The proposed framework consists of an initial segmentation based on a simple intensity filter on each individual image slice, which is used to generate an initial mesh model. Following this, an iterative deformable modelling process is implemented which deforms the initial mesh towards the lymphatic vessel wall. An overview of the proposed framework is shown in Figure 1. For full vessel segmentation, the segmentation framework is implemented twice; once for the outer wall and once for the inner wall; so that segmentation of both walls are

carried out independently.

The initial meshes are generated by first carrying out an initial segmentation on each individual image slice. These segmentation contours have the same number of points, making it possible to define edges between slices to generate a face-vertex mesh.

The deformable modelling process is iterative and stops when the maximum number of iterations is reached. This process consists of two components. Firstly a 2D boundary detector is carried out on each individual slice, where search paths are defined along the normal direction of each mesh vertex. A neural network is used for boundary detection in order to learn useful features, rather than spending time hand crafting them. Finally, 3D mesh regularisation is implemented on the entire mesh, using a B-spline-based method. This ensures a smooth surface not only on each 2D contour, but also between contours in the third dimension.

On every iteration the boundary detector's search path decreases in order to reach convergence, and the degrees of freedom associated with the mesh regularisation increases to allow the mesh to deform to areas of high curvature. As a result, the deformable modelling process can be thought of as an iterative refinement process.

2.1 Initial Segmentation

Before deformable modelling, an initial mesh model must be defined. This section describes an initial 2D intensity-based segmentation on a slice-by-slice basis, before combining the estimated 2D contours to generate a simple 3D mesh structure.

It is assumed that the pixel intensities within the lymphatic vessel walls are significantly higher than the remaining pixels, therefore it is assumed that the pixels with highest local gradient are on the boundary. To this end, a simple 2-rectangle Haar-like filter [17] is employed to highlight the pixels of high gradient. For every pixel in the image a filter response is computed as follows;

$$f = \sum_{k=0}^{N} \mu_1^k - \sum_{k=0}^{N} \mu_2^k \tag{1}$$

where μ_1^k is the intensity of pixel k in rectangle 1, μ_2^k is the intensity of pixel k in rectangle 2, and N is the number of pixels in each rectangle.

The filter is applied to the image in polar coordinates, and for each column in the polar image the pixel with the optimal filter response is identified. As the appearance of the outer and inner walls are opposite each other, so too will the filter response. Therefore the maximum value of Equation 1 is used to identify pixels on the inner wall, and the minimum value is used to identify outer wall pixels. A filter size of 1×21 is centred at the test pixel, where $N = 10$ pixels are summed in rectangle 1, and $N = 10$ pixels are also summed in rectangle 2. The

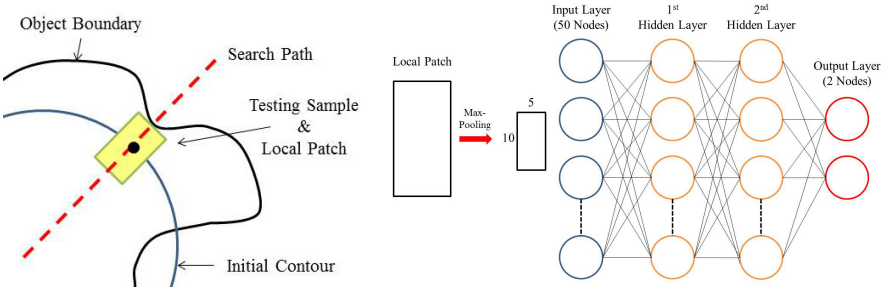

Fig. 2. Left: Schematic diagram of local patch intensity extraction. Right: Example NN architecture with 2 hidden layers.

contour in polar coordinates is then converted back to cartesian coordinates, and is smoothed by fitting the contour to an ellipse. This is done by optimising the conic equation for an ellipse using the least-squares algorithm.

This process is repeated for every slice in the 3D image. However, it is also assumed that the boundary walls do not significantly change between adjacent slices, therefore the smoothed contour from the previous slice is used to help estimate the contour on the next slice. This is done by restricting the search space for finding the optimal filter response in each polar image column. A contour point in column j in the polar image of slice $i+1$ must be within ± 10 of the contour point in column j in slice i.

Given that each slice was converted to polar images of the same size, the number of contour points on each slice is also equal. Therefore contour point j of slice i is correspondent to contour point j in slice $i+1$. This makes generating the mesh a simple task by simply defining mesh edges between corresponding contour points in adjacent slices.

2.2 Neural Network Boundary Detection

Search paths are defined along the inward and outward normals of each vertex of the initial mesh. The normal directions can be straightforwardly computed given the vertices' neighbours. Each search path coordinate is tested to get a boundary probability score, and the coordinate with the highest score on each path is considered the new vertex position.

Raw intensity values from a local patch are inputted into a NN for each search path coordinate. Layers of nodes are connected by weights, and each node is treated as a perceptron. Their activations are then calculated by passing their weighted sum of inputs through an activation function. Given a supervised output the weights are optimised using the *back-propagation* and *Levenberg-Marquardt* algorithms.

To ensure that the appearance of the boundary pixels' local patches are rotationally invariant, the local patch is aligned with the search path. This comes at no extra computational cost as the normal directions have already been computed in order to define the search paths. Local patches are down-sampled to reduce the number of network inputs, which subsequently speeds up the training process. *Max-pooling* is used for this purpose. The process involves sliding a non-overlapping pooling window across the image and extracting the maximum intensity value in each window. While this is an effective down-sampling technique, it also creates position invariance over larger local regions. The size of the pooling window and its stride are chosen to ensure a 10×5 output in all cases. The fully-connected neural network architecture is constructed in the conventional manner, with the 50 pixels of the local patch being represented by an input layer of 50 nodes. The output layer consists of 2 nodes representing boundary and non-boundary, essentially making this a binary classification problem. All nodes in adjacent layers are fully connected. A schematic diagram of the local patch extraction, and an example of a neural network architecture with 2 hidden layers are shown in Figure 2.

An additional smoothing process follows boundary detection. Given the assumption that both the inner and outer vessel walls are tubular in shape, any distant outliers from an ellipse-like shape on any slice are discarded, and are replaced by "interpolated" contour points. Given a 2D contour V containing n points after boundary detection, an ellipse is fitted which yields a new contour of n points, V_e. Outliers in V are identified if the distance to V_e is above threshold $t = 25$ pixels. Any outliers in V are then replaced by their nearest neighbour in V_e. This small step becomes important especially when detecting the boundary of the inner wall, where a valve-like structure is seen at the centre of the vessel. This avoids vertices converging near the valve instead of the inner vessel wall.

2.3 Segmentation with B-spline Mesh Regularisation

Before boundary detection, there is an original set of mesh vertices V, and after boundary detection there is now a new set of mesh vertices V'. As there is no shape restrictions in these components (apart from the length of the boundary detector search path itself), an additional process is needed to preserve the mesh's smooth surface. We use B-spline based mesh regularisation, where a local transformation $T(x, y, z)$ between V and V' is estimated with 3D B-splines. The transformation is then performed on V using free-form-deformation, so that it fits as close as possible to V'. As a result, the smoothness of the transformed mesh is a function of the number of B-spline degrees of freedom.

The FFD is estimated by warping an underlying voxel lattice controlled by a set of control points. The control points are defined as $\phi^h_{i,j,k}$ of size $n_x \times n_y \times n_z$,

which are separated by δ, and the FFD is formulated as follows;

$$T(x,y,z) = \sum_{l=0}^{3}\sum_{m=0}^{3}\sum_{n=0}^{3} B_l(u)B_m(v)B_n(w)\phi_{i+l,j+m,k+n} \tag{2}$$

where B_l represents the lth basis function of the B-spline. The voxel lattice positions are $i = \lfloor x/n_x \rfloor - 1$, $j = \lfloor y/n_y \rfloor - 1$, and $k = \lfloor z/n_z \rfloor - 1$. $u = x/n_x - \lfloor x/n_x \rfloor$, $v = y/n_y - \lfloor y/n_y \rfloor$, and $w = z/n_z - \lfloor z/n_z \rfloor$ are the fractional positions along the lattice [8]. In addition, the non-rigid transformation is estimated in a multi-resolution procedure which is expressed as a summation of FFDs at multiple resolutions H [8].

$$T^H(x,y,z) = \sum_{h=1}^{H} T^h(x,y,z) \tag{3}$$

At each mesh resolution h, the voxel lattice is warped by moving the set of control points $\phi^h_{i,j,k}$ which is consequential of δ_h, and computed is $\delta_h = \delta_0/2^h$, where δ_0 is the original control point spacing and h is the resolution level. The B-spline parameters $\phi^h_{i,j,k}$, are optimised by minimising the following energy function with gradient descent;

$$E(\phi) = E_s(V', V) + \lambda E_r(T), \tag{4}$$

where E_r is a smoothness cost and λ is a constant that defines the contribution of the smoothness term. E_s, is a similarity metric, which is a sum-of-squared-difference (SSD) metric between V and V'.

A high δ yields less control points that are sparsely separated, yielding less degrees of freedom. A low δ increases the number of control points, making interpolation distances shorter, yielding more degrees of freedom. A balance os found to allow V to deform as close to the boundary positions as possible (V'), while resulting in a sufficiently smooth surface. Two parameters are changed on every iteration in order to achieve such a trade-off. Firstly the boundary detector's search path decreases on every iteration, allowing the system to reach convergence more quickly. Secondly, as the amount of possible deformation is reduced at each iteration, it is less likely that the mesh surface will get tangled. Therefore on every iteration, the value of δ is also reduced.

3 Application and Results

The lymphatic vessel was labelled on six $512 \times 512 \times 512$ *ex-vivo* confocal microscopic volumes. For each volume the vessel's inner and outer wall were labelled on every tenth slice, and ground truth meshes were then generated by manually defining mesh edge connections. Inner and outer wall ground truths were obtained independently, and so all experimental results are also evaluated independently. Gaussian smoothing was applied to the image volumes in an attempt to remove noise, and all experiments were performed with leave-one-out cross-validation.

3.1 Boundary Detection Results

Before obtaining full segmentation, initial classification tests were carried out on several neural network architectures for boundary detection. The effect of the number of nodes in the network's first hidden layer, the total number of hidden layers, and the local patch size were analysed before deciding on an architecture for segmentation. In all cases 50,000 sample pixels were used for training, 50% of which were boundary (positive) and 50% non-boundary (negative). Search paths were defined for all ground truth vertices with a length of 30 pixels at either side. Non-boundary samples were randomly selected from these search paths. At the testing stage a search path of 30 pixels was also used, resulting in 61 path pixels for each point. All of the search path coordinates at this stage were classified as boundary or non-boundary.

Inner wall classification sensitivity and specificity from all initial tests ranged between 87%-92%, and 74%-85%, respectively, while outer wall sensitivity and specificity ranged between 87%-92% and 77%-87%. This indicates that at first attempt NNs can produce acceptable results for obscured lymphatic vessel boundary detection. The detectors' sensitivity values are significantly higher and have lower variance than their specificity, which is to be expected as the boundary region is highly diffused. Given this, it is important to find an architecture which produces the highest specificity results as possible to accurately classify non-boundary pixels close to the boundary.

Architectures with 1, 2, 5, 15, 40 and 100 nodes were tested. These tests showed little variance in the inner and outer wall's sensitivity (2% and 3% respectively), however the specificity variance was significant larger (11% and 10%). Furthermore the specificity for both walls increased with increasing nodes, and plateaued at 40 nodes with 85% and 87%. This suggests that a sufficient number of nodes is necessary to discriminate between boundary and non-boundary pixels. Architectures with 1, 2 and 3 layers were also tested, however increasing the layers had a marginal detrimental effect on the specificity of both walls ($\sim 2\%$), possibly due to overfitting. Given that the boundary area is diffused, highly abstract and complex features may be too specific for good generalisation, suggesting that a simple NN architecture of one hidden layer is sufficient for boundary detection. Networks were trained by extracting patch sizes of 20×10, 40×20 and 80×40 were also extracted, which showed that there was little difference between extracting larger patch sizes ($< 1\%$). However, there was a drop of 3% in the specificity of inner wall classification for the smallest patch, suggesting that a relatively large patch is needed to incorporate useful boundary features.

Based on these results a NN architecture was chosen for full segmentation. For simplicity the same architecture is used for both inner and outer walls. An architecture with 40 nodes in the first hidden layer is sufficient, and larger patches of 40×20 or 80×40 should be extracted due to their higher specificity for the vessel's inner wall. For simplicity and to reduce computation, the smaller of

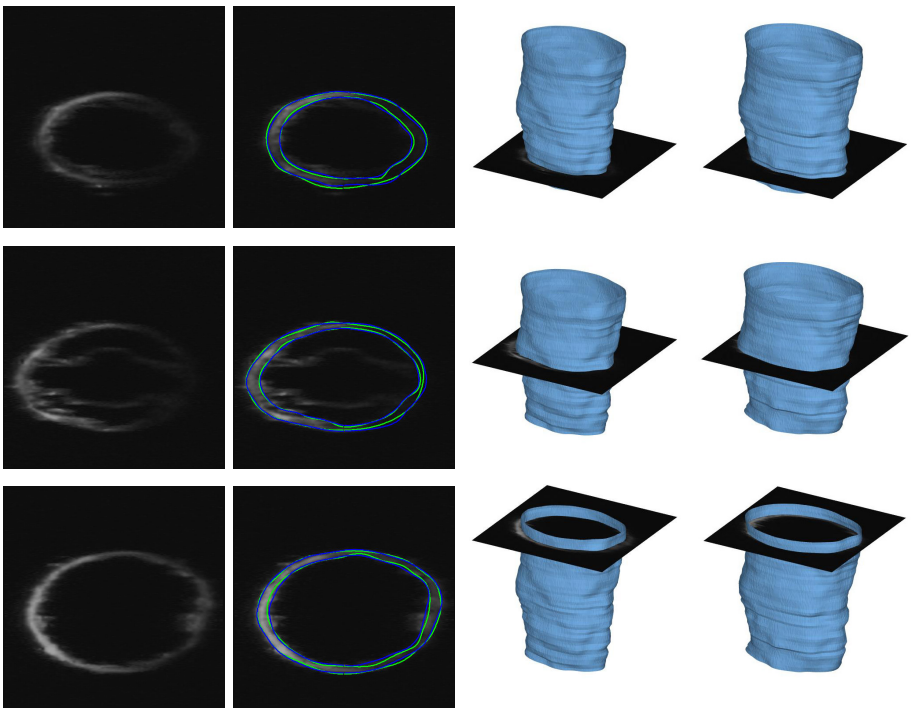

Fig. 3. Example segmentation results. From left to right; 1st column: Image slices. 2nd column: Inner and outer wall segmentation results. Green contours are the ground truth and blue contours are the result. 3rd column: Resulting inner wall mesh with corresponding slices. 4th column: Resulting outer wall mesh with corresponding slices.

the two was chosen. Finally a simple architecture of one hidden layer produced the best specificity results. To this end, the NN boundary detector used for segmentation has a single hidden layer of 40 nodes with local patch extraction of size 40×20. This architecture produced boundary sensitivities of $88 \pm 2\%$ and $91 \pm 4\%$ for the inner and outer walls receptively, and specificities of $85 \pm 3\%$ and $87 \pm 1\%$. Furthermore, the vast majority of incorrectly classified non-boundary pixels were in the immediate vicinity of the ground truth boundary. Given that the appearance of the vessel is diffused, classification errors would be expected in this small region.

3.2 Segmentation Results

The proposed method was compared to two alternative approaches, as well as our initial segmentation method. For fair comparison our results were only compared to other methods working on the same dataset. To our knowledge, Essa et al. [3] are the only others to do this, and so we compared our results to their *minimum s-excess* graph segmentation. This involved formulating a graph to segment both

Method	PMD (vox)	HD2 (vox)	AO (%)	Sens. (%)	Spec. (%)
S-Excess Graph [3]	3.1 ± 1.9	9.8 ± 4.3	95.5 ± 3.2	96.9 ± 3.1	99.2 ± 0.8
Intensity-based	5.9 ± 0.8	48.5 ± 7.1	92.4 ± 1.5	93.0 ± 1.4	99.1 ± 0.1
Initial Seg.	2.9 ± 0.4	9.3 ± 0.9	96.4 ± 0.4	97.0 ± 0.4	$\mathbf{99.6 \pm 0.1}$
Proposed	$\mathbf{1.6 \pm 0.1}$	$\mathbf{5.8 \pm 0.5}$	$\mathbf{98.0 \pm 0.4}$	$\mathbf{99.1 \pm 0.4}$	99.2 ± 0.2

Table 1. Inner wall quantitative results comparison.

Method	PMD (vox)	HD2 (vox)	AO (%)	Sens. (%)	Spec. (%)
S-Excess Graph [3]	2.0 ± 0.8	7.4 ± 3.1	97.6 ± 1.0	98.7 ± 1.1	99.1 ± 0.6
Intensity-based	4.5 ± 1.4	46.9 ± 8.1	95.0 ± 1.8	96.9 ± 1.4	98.3 ± 0.8
Initial Seg.	1.7 ± 0.2	5.7 ± 0.3	98.2 ± 0.1	99.2 ± 0.1	99.0 ± 0.3
Proposed	$\mathbf{1.5 \pm 0.1}$	$\mathbf{5.4 \pm 0.4}$	$\mathbf{98.4 \pm 0.1}$	$\mathbf{99.2 \pm 0.2}$	$\mathbf{99.2 \pm 0.03}$

Table 2. Outer wall quantitative results comparison.

inner and outer walls simultaneously in polar coordinates, and a hidden Markov model was used to track the vessel walls between the columns. Secondly, a simple intensity-based approach was implemented using Haar-like filtering. This was the same filtering used in Section 2.1, but without contour smoothing in the cartesian coordinate system. For the remainder of this paper this approach is referred to as *intensity-based* segmentation. In doing this we have allowed comparison with a purely data-driven approach which had no shape regularisation, and to a completely different segmentation approach. Evaluation was performed on a 2D slice-by-slice basis in polar coordinates. The point-to-mesh distance (PMD), Hausdorff distance (HD), area overlap (AO), and foreground and background specificity and sensitivity were the metrics used.

Figure 3 shows an example segmentation of the proposed method, which shows close correlation with the ground truth. Smooth resulting mesh surfaces are also shown, with no tangled or extremely faceted mesh faces. Tables 1 and 2 show that the proposed method produced the lowest PMD and HD, and the highest AO, specificity and sensitivity results. Figures 4 and 5 compare the qualitative slice segmentations and mesh results for the inner and outer walls of the data-driven approaches.

It is immediately noticeable that the simplistic intensity-based segmentation produced significantly worse quantitative results, and large regions of both walls deviated significantly from the ground truth. Noticeably, the boundary detector has caused inner wall vertices to converge at the valve at the centre of the vessel, as its appearance is similar to the wall itself. The lack of any shape regularisation is therefore unsuitable for such data where the vessel walls are not always prominent. The initial segmentation results are significantly better. By fitting each slice contour to an ellipse the majority of *correctly* deviated vertices have forced the *incorrectly* placed vertices nearer the boundary walls. This simple shape regularisation approach has had dramatic effects on the smoothness

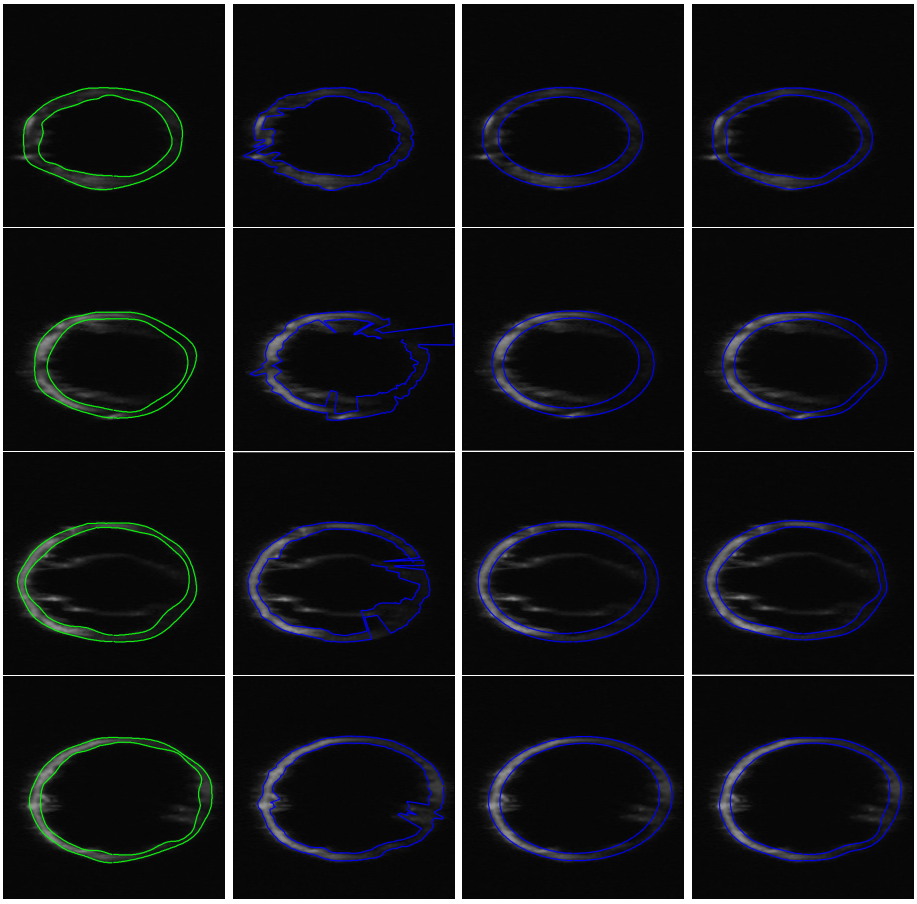

Fig. 4. Comparison results on image slices. From left to right; 1st column: Ground truth. 2nd column: Intensity-based segmentation. 3rd column: Initial segmentation. 4th column: Proposed framework.

of the mesh surface, however it does not allow enough degrees of freedom to reach boundary areas of high curvature. The results from the proposed method show that the additional deformable modelling process is necessary after initial segmentation. The iterative boundary detector allows deformation towards areas of high curvature, which is represented by both the low PMD and HD errors. Meanwhile the iterative mesh regularisation maintains the mesh's smooth surface, which can be seen in Figure 5.

Compared to the minimum s-excess graph method, the proposed method still produced better segmentation results. The tracking-based method produced PMD and HD metrics that were higher for the outer wall, and almost double that of the proposed method for the inner wall. This is also reflected in the AO, specificity and sensitivity metrics. This may be a result of the tracking

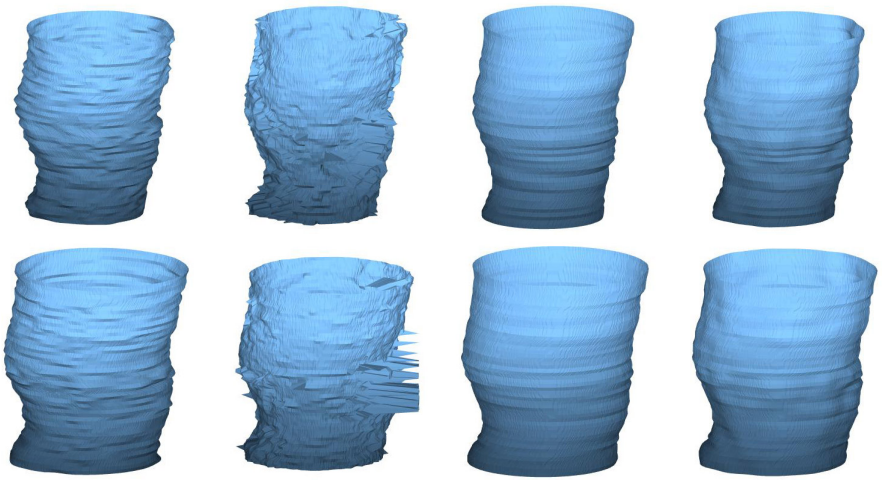

Fig. 5. Comparison mesh results. The top row shows the inner vessel wall mesh and the bottom row shows the outer wall mesh. From left to right; 1st column: Ground truth. 2nd column: Intensity-based segmentation. 3rd column: Initial segmentation. 4th column: Proposed framework.

model, however a likely cause is the hand-crafted edge features used for emission probability. This being the case it would show that using learned features from algorithms such as NN has an advantage for edge detection in such data.

4 Conclusion

A fully automatic deformable modelling method has been presented for the segmentation of 3D lymphatic vessels in confocal microscopy images. A bottom-up, data-driven framework was used, which included a learning-based boundary detector and mesh regularisation for shape preservation. A simple intensity-based initial segmentation was first adopted which was followed by a deformable modelling system. A neural network was used for boundary detection, which allowed suitable features to be learned instead of hand-crafting them. This proved particularly useful, as choosing features for edges with varying degrees of contrast is not a trivial task. It was also shown that this type of boundary detection was able to accurately detect both vessel walls, proving it was capable of detecting edges of highly varying contrasts. Mesh regularisation was also necessary in order to obtain smooth vessel surfaces.

References

1. Chiverton, J., Xie, X., Mirmehdi, M.: Automatic bootstrapping and tracking of object contours. IEEE T-IP 21(3), 1231–1245 (2012)

2. Espona, L., Carreira, M., Penedo, M., Ortega, M.: Retinal vessel tree segmentation using a deformable contour model. In: ICPR. pp. 2128–2131 (2008)
3. Essa, E., Xie, X., Jones, J.L.: Minimum s-excess graph for segmenting and tracking multiple borders with hmm. In: MICCAI. pp. 28–35 (2015)
4. Hu, Y., Rogers, W., Coast, D., Kramer, C., Reichek, N.: Vessel boundary extraction based on a global and local deformable physical model with variable stiffness. MRI 16, 943–951 (1998)
5. Jones, J., Essa, E., Xie, X., Smith, D.: Interactive segmentation of media-adventitia border in IVUS. In: CAIP. pp. 466–474 (2013)
6. Jones, J., Xie, X., Essa, E.: Combining region-based and imprecise boundary-based cues for interactive medical image segmentation. J. Numerical Methods in Biomedical Engineering 30(12), 1649–1666 (2014)
7. Kirbas, C., Quek, F.: A review of vessel extraction techniques and algorithms. ACM Computing Surveys (CSUR) 36(2), 81–121 (2004)
8. Lee, S., Wolberg, G., Shin, S.Y.: Scattered data interpolation with multilevel b-splines. Trans. Visualization and Computer Graphics 183(3) (1997)
9. Lesage, D., Angelini, E.D., Bloch, I., Funka-Lea, G.: A review of 3d vessel lumen segmentation techniques: Models, features and extraction schemes. Medical image analysis 13(6), 819–845 (2009)
10. Lu, D., Yu, X., Jin, X., Li, B., Chen, Q., Zhu, J.: Neural network based edge detection for automated medical diagnosis. In: IEEE ICIA. pp. 343–348 (2011)
11. Ma, J., Lu, L., Zhan, Y., Zhou, X., Salganicoff, M., Krishnan, A.: Hierarchical segmentation and identification of thoracic vertebra using learning-based edge detection and coarse-to-fine deformable model. In: MICCAI 2010, pp. 19–27 (2010)
12. McInerney, T., Terzopoulos, D.: Deformable models in medical image analysis: A survey. MIA 1(2), 91–108 (1996)
13. Mesejo, P., Ibáñez, O., Cordón, O., Cagnoni, S.: A survey on image segmentation using metaheuristic-based deformable models: state of the art and critical analysis. Applied Soft Computing 44, 1–29 (2016)
14. Paiement, A., Mirmehdi, M., Xie, X., Hamilton, M.: Integrated segmentation and interpolation of sparse data. IEEE T-IP 23(11), 3902–3914 (2014)
15. Palmer, R., Xie, X., Tam, G.: Automatic aortic root segmentation with shape constraints and mesh regularisation. In: BMVC (2015)
16. Senthilkumaran, N., Rajesh, R.: Edge detection techniques for image segmentation–a survey of soft computing approaches. IJRTE 1(2) (2009)
17. Viola, P., Jones, M.: Rapid object detection using a boosted cascade of simple features. In: Proc. Conf. Computer Vision and Pattern Recognition. pp. 511–518 (2001)
18. Xie, X., Mirmehdi, M.: Magnetostatic field for the active contour model: A study in convergence. In: BMVC. pp. 127–136 (2006)
19. Xie, X., Mirmehdi, M.: Implicit active model using radial basis function interpolated level sets. In: BMVC. pp. 1–10 (2007)
20. Yeo, S., Xie, X., Sazonov, I., Nithiarasu, P.: Level set segmentation with robust image gradient energy and statistical shape prior. In: IEEE ICIP (2011)
21. Yim, P., Cebral, R., Mullick, R., Choyle, P.: Vessel surface reconstruction with a tubular deformable model. IEEE T-MI 20, 1411–1421 (2001)